Towards Clinical Application of a Laplace Operator-based Region of Interest Reconstruction Algorithm in C-arm CT

Yan Xia, *Student Member, IEEE*, Hannes Hofmann, Frank Dennerlein, Kerstin Mueller, *Student Member, IEEE*, Chris Schwemmer, Sebastian Bauer, Gouthami Chintalapani, Ponraj Chinnadurai, Joachim Hornegger, *Member, IEEE*, and Andreas Maier, *Member, IEEE*

***Abstract*—It is known that a reduction of the field of view (FOV) in 3D X-ray imaging is proportional to a reduction in radiation dose. The resulting truncation, however, is incompatible with conventional reconstruction algorithms. Recently, a novel method for region of interest (ROI) reconstruction that uses neither prior knowledge nor extrapolation has been published, named Approximated Truncation Robust Algorithm for Computed Tomography (ATRACT). It is based on a decomposition of the standard ramp filter into a 2D Laplace filtering and a 2D Radon-based residual filtering step. In this paper, we present two variants of the original ATRACT. One is based on expressing the residual filter as an efficient 2D convolution with an analytically derived kernel. The second variant is to apply ATRACT in 1D to further reduce computational complexity. The proposed algorithms were evaluated by using a reconstruction benchmark, as well as two clinical data sets. The results are encouraging since the proposed algorithms achieve a speed-up factor of up to 245 compared to the 2D Radon-based ATRACT. Reconstructions of high accuracy are obtained, e.g. even real-data reconstruction in the presence of severe truncation achieve a relative root mean square error (rRMSE) of as little as 0.92 % with respect to non-truncated data.**

***Index Terms*—C-arm CT, dose reduction, image reconstruction, region of interest, truncation, truncation artifact**

I. Introduction

MANY interventional procedures in neuroradiology involve minimally-invasive techniques that require image guidance, often provided by two-dimensional (2D) digital subtraction angiography (DSA) on flat-panel C-arm system. 2D DSA images provide excellent spatial resolution but lack both low-contrast resolution and three-dimensional (3D) anatomical information [1]. This may cause difficulties when localizing the devices within the treatment region. 3D C-arm imaging, on the other hand, offers both low-contrast resolution and 3D spatial orientation, and was found to be a valuable imaging tool during the therapy of intracranial aneurysms [2], [3], [4]. Fig. 1 illustrates the localization of a deployed pipeline stent with respect to the treatment region in 2D angiography and 3D imaging.

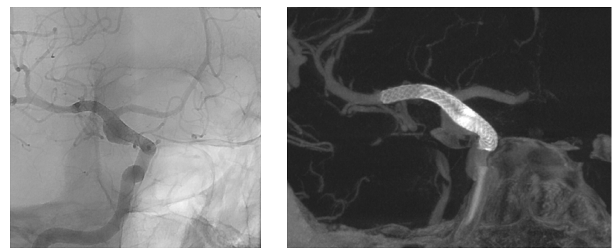

(a) (b)

Fig. 1: Visualization of a deployed neurological stent with respect to the treatment region in (a) view-aligned 2D angiography, and (b) rendered volume from 3D imaging (Images courtesy of St. Luke's Episcopal Hospital, Houston, TX, USA).

However, radiation dose to the patient can be substantial during a low contrast 3D scan [5]. Therefore, a reduction in radiation dose without compromising image quality in C-arm CT has become an active field of research for such circumstances. In some clinical applications and workflows (e.g. examination of deployed stents or coils during the intervention, cochlear implants, and needle biopsies) only a small portion of the patient may be of diagnostic interest. This enables the idea of 3D region of interest (ROI) imaging, utilizing an X-ray beam collimator to transaxially and axially block radiation during image acquisition. This approach yields a significant reduction of patient dose, but the resulting projection truncation typically leads to severe artifacts when using conventional CT algorithms. These artifacts manifest as a bright ring at the edges of the 3D ROI and will dramatically contaminate the image quality in the reconstruction results.

Therefore, it is of practical significance to develop an algorithm for 3D ROI imaging that is of comparable accuracy to reconstructions from non-truncated data. In addition to high image quality, we are also interested in an algorithm that is suitable for any clinical workflow. The algorithm should pose as little constraints on the availability of prior image data such

Y. Xia, H. Hofmann, K. Mueller, C. Schwemmer, J. Hornegger and A. Maier are with the Pattern Recognition Lab, Friedrich-Alexander-University Erlangen-Nuremberg, 91058 Erlangen, Germany. Y. Xia, K. Mueller, C. Schwemmer and J. Hornegger are also with the Erlangen Graduate School in Advanced Optical Technologies (SAOT), Friedrich-Alexander-University Erlangen-Nuremberg, 91052 Erlangen, Germany. (e-mail: yan.xia@cs.fau.de; hannes.hofmann@cs.fau.de; kerstin.mueller@cs.fau.de; chris.schwemmer@cs.fau.de; joachim.hornegger@cs.fau.de; andreas.maier@cs.fau.de).

F. Dennerlein and S. Bauer are with Siemens AG, Healthcare Sector, 91052 Erlangen, Germany (e-mail: frank.dennerlein@siemens.com; sebastian-bauer@siemens.com).

G. Chintalapani and P. Chinnadurai are with Siemens Medical Solutions USA Inc., Hoffman Estates, IL, USA (e-mail: gouthami.chintalapani@siemens.com; ponraj.chinnadurai@siemens.com).

as preoperative scans and prior image information collected during the intervention as possible. Any such constraint would immediately imply a restriction of the applicability of the algorithm to a workflow that provides exactly the required data. Furthermore, no additional low-dose data should be required, as the delay caused by patient repositioning and the acquisition itself introduces another burden on the interventional operator and impairs the ease of use of the method.

II. Related Work

Various approaches concerning the correction of truncation have been proposed in the literature over the last several years.

One category requires prior knowledge about the reconstructed object but achieves an exact reconstruction of the object ROI if some geometrical conditions are satisfied by the imaging configuration. Corresponding algorithms were suggested by Noo et al. [6] and Pan et al. [7] and are based on the concept of Differentiated Backprojection (DBP): After backprojecting the derivative of the projection data, these methods require a 1D finite Hilbert inversion along specific lines in the backprojection result. Later, Defrise et al. [8], Ye et al. [9], [10], and Kudo et al. [11] suggested an extension to the DBP method that solves the Hilbert inversion by iterative projection onto convex sets (POCS). This extension allows a wider class of truncation configurations to be solved accurately, but at the cost of higher computational efforts.

Yu et al. [12] and Cho et al. [13] adapted the PI-line-based backprojection filtration (BPF) algorithm from helical cone-beam CT to a circular geometry. In this method, the PI-line support segment can be small and only the data backprojected onto the PI-line support segment is required to reconstruct the image, which enables the ROI image reconstruction.

Chityala et al. [14], Chen et al. [15] and Schafer et al. [16] suggested to use a filtering mask between the X-ray source and the patient, to reduce rather than completely block radiation outside the ROI. Therefore, projections will not be truncated, but data acquisition becomes more complex and dose reduction benefits might be reduced. Alternatively, patient size, shape and attenuation information can also be obtained from a prior low-dose CT scan (Kolditz et al. [17], [18]), if available, and then used to extend the collimated projections outside the ROI.

Another major category of ROI reconstruction methods is based on estimating the missing data using an extrapolation procedure, such as symmetric mirroring of projection images (Ohnesorge et al. [19]), water cylinder/ellipse extrapolation (Hsieh et al. [20], Maltz et al. [21]), smooth function estimation (Van Gompel et al. [22]), square root extrapolation (Sourbelle et al. [23]), optimization-based extrapolation (Maier et al. [24]) or scattering radiation-based extrapolation (Bier et al. [25]). However, these methods are based on heuristic assumptions that may not always accurately approximate the objects outside the ROI.

Iterative reconstruction can also be a candidate for tackling the interior problem. Some related work focusing on the use of compressed sensing (Yu et al. [26]) and total variation (Yang et al. [27]) was also suggested.

Recently, another filtered-backprojection method (ATRACT) has been proposed for ROI reconstruction from transaxially-truncated projections (Dennerlein [28]). This algorithm neither uses prior knowledge nor explicit extrapolation and no hardware changes in the acquisition systems are needed. It therefore goes along with the workflow requirements described in the previous section and can readily be applied on current clinical C-arm systems. The ATRACT reconstruction scheme was originally derived in [28] using 2D Radon transform operations. We thus refer to this method as 2D Radon-based ATRACT throughout this paper. This algorithm, however, requires frequent interpolations and complicates the filtering procedure. For practical use, ATRACT was later refined to a more practically-useful reconstruction algorithm with implementations that are based on a 2D convolution. The corresponding kernel was numerically determined in [29], [30] and analytically derived in [31]. To further reduce the computational complexity, ATRACT coming with non-local row-wise filtering was suggested, with a 1D kernel numerically determined by computing the impulse response of the standard ramp filtering coupled with the second-order anti-derivative operator [32]. Note that all of the previous algorithms suffer from a global offset problem. To tackle this problem, two solutions [33], [34] were suggested and evaluated on synthetic data.

In this paper we present the analytical derivations of 2D and 1D convolution-based ATRACT. Both result in a noticeable computational speed-up and thus make ROI imaging applicable to interventional workflows. Furthermore, we present the steps that need to be undertaken to make these algorithms suitable for clinical application. The performance of a refined heuristic extrapolation method [35] was also investigated and compared to our proposed algorithms. In the experimental part, image quality evaluations involving both virtually cropped and physically collimated clinical datasets are provided.

III. Truncation Correction

A. CB Projection and Truncation

Let us denote the object density function $f(\mathbf{x})$ with $\mathbf{x} = (x, y, z)$. Focus on the circular cone-beam (CB) imaging geometry with a flat-panel detector shown in Fig. 2, the 2D projection at the rotation angle λ obtained for all possible unit vectors $\boldsymbol{\alpha}$ can be written as

$$g(\lambda, u, v) = \int_{0}^{\infty} f(\mathbf{a}(\lambda) + t\boldsymbol{\alpha}(\lambda, u, v))\, \mathrm{d}t\,. \tag{1}$$

The reconstruction problem is to restore $f(\mathbf{x})$ from CB data $g(\lambda, u, v)$ collected over a suitable angular range, e.g., of π plus fan-beam angle in a short-scan acquisition. The Feldkamp–Davis–Kress algorithm (FDK) [36] is commonly used for the circular cone-beam reconstruction due to its simplicity and efficiency. It typically consists of the following three steps: 1) Cosine and Parker weighting of the projection data to obtain $g_1(\lambda, u, v)$; 2) a row-wise ramp filtering of pre-weighted data to get the filtered projection data $g_F(\lambda, u, v)$; 3) a distance weighted cone-beam backprojection to restore the object function $f(\mathbf{x})$. Because of the non-local property of the ramp kernel, filtering of any point of a projection

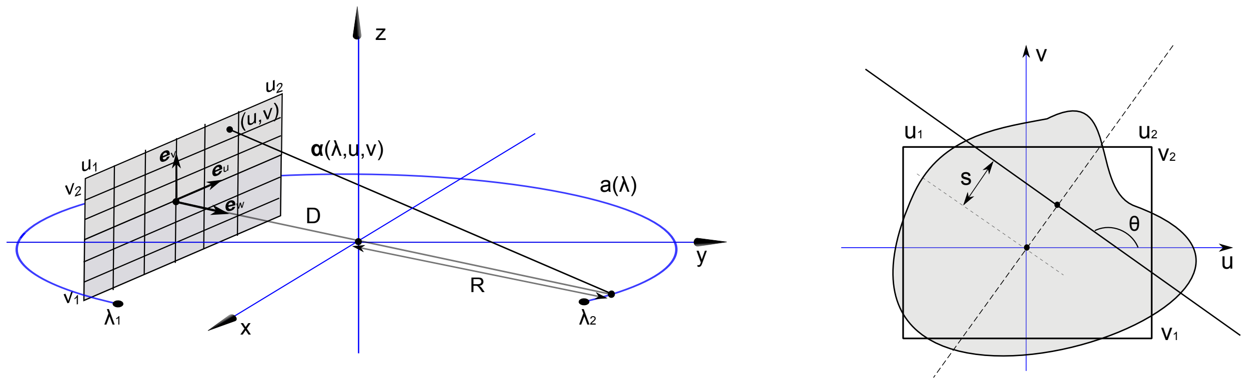

(a) (b)

Fig. 2: Geometry and associated notations. (a) Short-scan circular cone-beam geometry with a flat-panel detector. (b) Detector coordinates (u, v) and Radon-based coordinates (θ, s). Notations: $\mathbf{a}(\lambda) = (R\cos\lambda, R\sin\lambda, 0)$ describes the trajectory of the X-ray source, with the patient-detector distance R and the rotation angle λ. $\mathbf{e_w}(\lambda)$ is the unit vector orthognoal to the flat-panel detector, and $\mathbf{e_u}(\lambda)$ and $\mathbf{e_v}(\lambda)$ are the orthogonal unit vectors at distance D from the source. $g(\lambda, u, v)$ denotes the projection data at the point (u, v) acquired at angle λ.

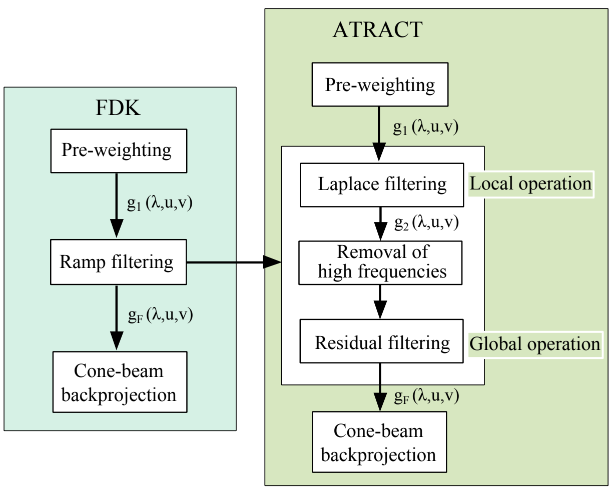

Fig. 3: Workflow of the FDK algorithm and the ATRACT algorithm. Note that ATRACT has the same first and last step as FDK, but comes with two successive 2D filtering steps instead of a row-wise ramp filtering. g_1, g_2 and g_F in ATRACT workflow indicate the projection data after pre-weighting (Cosine and Parker weighting), Laplace filtering and residual filtering, respectively.

image requires the knowledge of all line integrals along the whole detector row. This requirement, however, is not satisfied anymore if projection data are transaxially truncated. Therefore, using standard FDK directly for reconstruction of truncated data will introduce severe artifacts, such as cupping artifacts and incorrect HU values.

B. 2D Radon-based ATRACT

In this section, we review the ATRACT reconstruction scheme that was originally derived in Ref. [28] using 2D Radon transform operations and that was later refined to a more practically-useful reconstruction algorithm [29]. The main idea was to find an equivalent of the 1D ramp filter within FDK so that the filtering procedure is intrinsically less sensitive to data truncation. The ramp filtering of $g_1(\lambda, u, v)$ is analytically reformulated to the 2D Laplace operation $(g_1(\lambda, u, v) \rightarrow g_2(\lambda, u, v))$ and a 2D residual filtering operation $(g_2(\lambda, u, v) \rightarrow g_F(\lambda, u, v))$ that is given by equations (20) and (21) in [28]. These equations define a 2D parallel-beam Radon transform, a angular weighting and a 2D backprojection, namely:

$$g_3(\lambda, \theta, s) = \int_{\Omega} g_2(\lambda, u, v)\, \delta\left(\mathbf{u} \cdot \begin{pmatrix} \cos\theta \\ \sin\theta \end{pmatrix} - s\right) \mathbf{du}\,, \quad (2)$$

$$g_F(\lambda, u, v) = -\frac{1}{4\pi^2}\frac{R}{D}\int_0^{\pi} |\cos\theta| g_3(\lambda, \theta, s^*)\, \mathrm{d}\theta \quad (3)$$

where $g_2(\lambda, u, v)$ indicates the pre-weighted projection data after the Laplace operation, $g_3(\lambda, \theta, s)$ is an intermediate function with the Radon-based coordinate, Ω indicates the shadow of the object on the detector, $\mathbf{u} = (u, v)$ and $s^* = u\cos\theta + v\sin\theta$.

The algorithmic flowchart of ATRACT is illustrated in Fig. 3, where it is compared to that of the short-scan FDK. The advantages of considering this two-step filtering can be summarized as follows:

1) The local 2D Laplace operation only introduces errors at the boundaries of the FOV, where outer neighboring values are unknown due to truncation, but nowhere else inside the FOV. In the numerical implementation, we remove any incorrect values at the FOV boundaries by setting them to zeros after Laplace filtering. With the FDK method, such a removal is not straightforward, due to the non-local character of the ramp filter.

2) Implicit extrapolation with zeros beyond the FOV boundaries in the second-order derivative domain yields a better approximation for the missing data than such an implicit extrapolation on $g(\lambda, u, v)$ or $g_1(\lambda, u, v)$, i.e. before differentiation.

3) Although the 2D Radon-based filtering is a non-local

operation, it is less sensitive to data inconsistencies than the 1D ramp filtering. Furthermore, as the 2D filtering is performed for all detector elements simultaneously, this reduces outliers that may be caused by individual 1D processing of detector lines.

Consequently, even though no explicit extrapolation is used during the filtering steps in ATRACT, the filtered result g_F will not contain a noticeable artificial structure at the edge of transaxial truncation compared to that of FDK method.

C. 2D Convolution-based ATRACT

A numerical implementation of ATRACT that directly adopts Eqns. (2) and (3) for the non-local residual filtering is computationally very expensive, because a 2D Radon transform and Radon inversion have to be executed once for each projection image. Moreover, Eqns. (2) and (3) require frequent interpolations, so a loss of spatial resolution in the reconstruction is unavoidable. For practical use of ATRACT, an implementation of the non-local filtering operation using a 2D convolution in u and v was suggested to increase computational efficiency [29], where the corresponding 2D kernel function was determined numerically by computing the 2D impulse response of (2) and (3).

Here we go one step further and analytically derive the convolution formula that replaces the 2D Radon-based filter in the original ATRACT algorithm. This analytical formula has the potential to increase spatial resolution in the ATRACT reconstructions and again significantly increases computational performance (due to FFT-based computations) compared to a direct implementation using (2) and (3). We refer to the new method as 2D ATRACT in the following.

With a small modification, Eqn. (2) can be rewritten as follows:

$$g_3(\lambda, \theta, s) = \int_{-\infty}^{\infty} g_2(\lambda, s\cos\theta - t\sin\theta, s\sin\theta + t\cos\theta)\,\mathrm{d}t\,. \tag{4}$$

Inserting (4) into (3) yields

$$g_F^{(ATRACT)}(\lambda, u, v) = -\frac{1}{4\pi^2}\frac{R}{D}\int_0^{\pi} |\cos\theta| \int_{-\infty}^{\infty} g_2(\lambda, s^*\cos\theta - t\sin\theta, s^*\sin\theta + t\cos\theta)\,\mathrm{d}t\mathrm{d}\theta\,. \tag{5}$$

Substituting variables (t, θ) by (u', v') with $u' = t\sin\theta$ and $v' = -t\cos\theta$, it is easy to obtain the following equations:

$$|t| = \sqrt{u'^2 + v'^2} \qquad \text{and} \tag{6}$$

$$\cos\theta = \frac{v'}{\sqrt{u'^2 + v'^2}}\,. \tag{7}$$

The area element $\mathrm{d}t\mathrm{d}\theta$ can be replaced by $|\mathbf{J}|\mathrm{d}u'\mathrm{d}v'$, where $|\mathbf{J}|$ is the determinant of the Jacobian, i.e.,

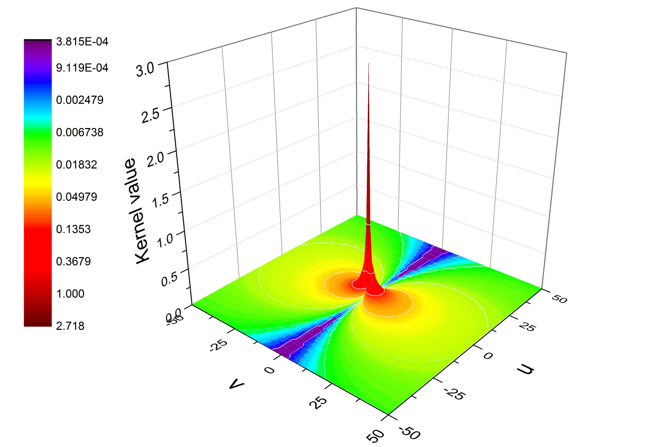

Fig. 4: 3D plot of the analytical 2D kernel in the spatial domain. The constant C_1 is set to 1. Note that in the numerical implementation, the singularity at $(u = 0, v = 0)$ can be approximated as the mean value of its neighboring points.

$$|\mathbf{J}| = \frac{1}{|\mathbf{J}|^{-1}} = 1/\det\left(\frac{\partial(t,\theta)}{\partial(u',v')}\right) = 1/\begin{vmatrix} \frac{\partial t}{\partial u'} & \frac{\partial \theta}{\partial u'} \\ \frac{\partial t}{\partial v'} & \frac{\partial \theta}{\partial v'} \end{vmatrix}$$
$$= 1/\begin{vmatrix} \sin\theta & -\cos\theta \\ t\cos\theta & t\sin \end{vmatrix} = 1/t. \tag{8}$$

Also, since $s^* = u\cos\theta + v\sin\theta$ and $\tan\theta = u/v$, we can obtain

$$s^*\cos\theta = u\cos^2\theta + u\frac{\sin\theta}{\cos\theta}\sin\theta\cos\theta = u\,, \tag{9}$$

$$s^*\sin\theta = v\frac{\cos\theta}{\sin\theta}\sin\theta\cos\theta + v\sin^2\theta = v\,. \tag{10}$$

Now, inserting (6), (7), (8), (9) and (10) into (5), we finally obtain the 2D convolution formula:

$$g_F^{(ATRACT)}(\lambda, u, v) = \int_{u_1}^{u_2}\int_{v_1}^{v_2} g_2(\lambda, u - u', v - v')\, h_{2D}(u', v')\,\mathrm{d}u'\mathrm{d}v'\,, \tag{11}$$

where the analytical 2D kernel $h_{2D}(u', v')$ is determined as follows:

$$h_{2D}(u', v') = -\frac{1}{4\pi^2}\frac{R}{D}|\cos\theta||\mathbf{J}| = C_1\frac{|v'|}{u'^2 + v'^2} \tag{12}$$

with $C_1 = -R/(4\pi^2 D)$.

The plot of the 2D analytical kernel is given in Fig. 4. A similar kernel was also found in the field of phase contrast CT [37].

The frequency representation of the analytical 2D kernel is given as

$$H_{2D}(\omega_u, \omega_v) = C_1\frac{|\omega_u|}{\omega_u^2 + \omega_v^2}\,. \tag{13}$$

where $H_{2D}(\omega_u, \omega_v)$ denotes the 2D Fourier transform of $h_{2D}(u, v)$; see the appendix for the derivation.

Now we can explain the reason why the ATRACT residual filtering is less affected by data inconsistencies. As shown in

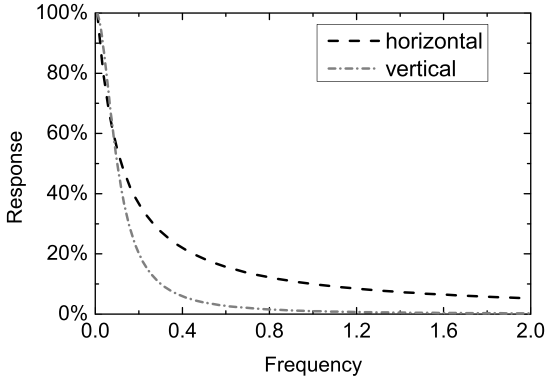

Fig. 5: Normalized line profiles of the 2D residual kernel in the Fourier domain. Frequency response shows that the 2D kernel possesses a low-pass character, which is able to provide a regularizing effect to suppress inconsistencies introduced in truncated data.

Fig. 5, the residual filter is a low-pass filter. This is beneficial since the data function $g_2(\lambda, u, v)$ contains inconsistencies due to implicit constant extrapolation to zeros outside the FOV, the filtering will provide a regularizing effect that is able to suppress these newly introduced inconsistencies in the projection image. Fig. 6 exemplarily shows different impacts of projection truncation on the 1D ramp filtering and 2D ATRACT filtering. As can be seen, the two-step ATRACT filtering can produce a more robust result than that of the ramp filtering in terms of eliminating the truncation-induced cupping artifact. The cupping artifact can be roughly quantified by the mean value difference between the two ROIs indicated in Fig. 6, with 14.8 for the ramp filter but only 0.07 for the two-step ATRACT filter. However, we found that 2D ATRACT filtering suffers an offset or bias-like artifact. This problem will be further addressed in Section III-D.

D. ATRACT with Row-wise Filtering

For further improvements in filtering speed, we will derive and investigate a 1D version of ATRACT. It is known that the computational complexity of a 2D FFT for a $N \times N$ image is proportional to $N^2 \log_2 N^2$, i.e. $2 \cdot N^2 \log_2 N$. Applying a 1D FFT to each row of the same image yields a complexity of $N \cdot N \log_2 N$, which implies a reduction of a factor of 2. Moreover, additional padding in the axial direction, as would be required for the 2D FFT-based filtering, is avoided. This contributes to further reduction of computation time when using 1D row-wise filtering.

We will derive the 1D ATRACT method starting with an alternative decomposition of the ramp filter. Radon's inversion formula is also referred to as the Differentiation, Hilbert transform and Backprojection (DHB) [6] which decomposes the ramp filter into two parts as follows

$$g_F^{(ATRACT)}(\lambda, u, v) = \frac{\partial g_1(\lambda, u, v)}{\partial u} * \frac{1}{2\pi^2 u}, \tag{14}$$

where the symbol * denotes the 1D convolution operation.

To derive the 1D ATRACT algorithm, Eqn. (14) can be modified as

$$g_F^{(ATRACT)}(\lambda, u, v) = \int_{-\infty}^{u} \frac{\partial^2 g_1(\lambda, \widetilde{u}, v)}{\partial \widetilde{u}^2} \mathrm{d}\widetilde{u} * \frac{1}{2\pi^2 u}. \tag{15}$$

Using the property of convolution, we can move the anti-derivative operator to the Hilbert kernel

$$g_F^{(ATRACT)}(\lambda, u, v) = \frac{\partial^2 g_1(\lambda, u, v)}{\partial u^2} * \int_{-\infty}^{u} \frac{1}{2\pi^2 \widetilde{u}} \mathrm{d}\widetilde{u}. \tag{16}$$

The first part of (16) is the 1D Laplace operation, i.e. the second-order derivative with respect to u (detector row) and the second integral can be further computed as follows

$$\begin{aligned}\int_{-\infty}^{u} \frac{1}{2\pi^2 \widetilde{u}} \mathrm{d}\widetilde{u} &= \int_{-\infty}^{1} \frac{1}{2\pi^2 \widetilde{u}} \mathrm{d}\widetilde{u} + \int_{1}^{u} \frac{1}{2\pi^2 \widetilde{u}} \mathrm{d}\widetilde{u} \\ &= C_2 + \frac{1}{2\pi^2} \ln|u|, \end{aligned} \tag{17}$$

where C_2 is a constant that is determined as

$$C_2 = \int_{-\infty}^{1} \frac{1}{2\pi^2 \widetilde{u}} \mathrm{d}\widetilde{u} \tag{18}$$

The expression of the 1D analytical kernel in the Fourier domain can be obtained by using Fourier transform of $\ln|u|$, which yields:

$$\begin{aligned} H_{1D}(\omega_u) &= \int_{-\infty}^{-\infty} \frac{1}{2\pi^2} \ln|u| e^{-i2\pi u \omega_u} \mathrm{d}u \\ &= -\frac{1}{4\pi^2} \frac{|\omega_u|}{\omega_u^2}. \end{aligned} \tag{19}$$

It can be observed that analogous to the 2D kernel, the 1D residual kernel possesses a low-pass property and its plot in the Fourier domain is consistent to the horizontal line profile in Fig. 5. Similarly, we analyze the filtering of 1D ATRACT from a truncated projection using the same configuration as in shown Fig. 6. As expected, 1D ATRACT filtering is superior to the standard 1D ramp filtering for removing inhomogeneous structural artifacts (achieves a mean value difference of 0.05 between the two ROIs) although both use a row-wise filtering to improve the runtime.

E. Offset Artifact in ATRACT

As mentioned in the previous sections, the 2D/1D ATRACT filtering is capable of eliminating truncation-induced cupping artifacts but an offset or bias-like artifact arises. This is because during the filtering process the mean value of the truncated projection data is removed. Thus, subsequent backprojection will be only correct up to an offset.

Throughout this paper we use the term "given scenario" to indicate the same acquisition geometry and same anatomical region of the patients, e.g. patient head scan. Depending on

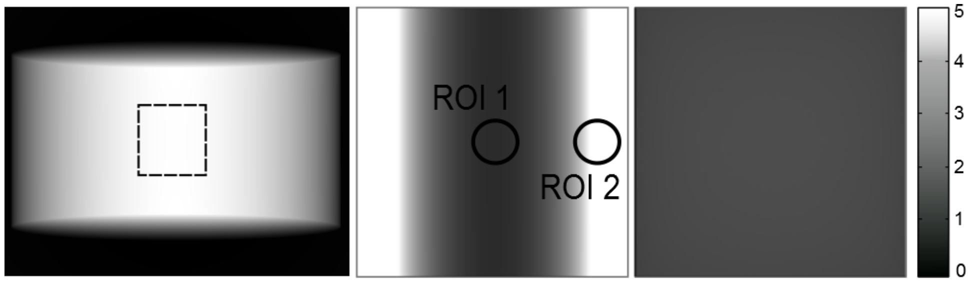

Fig. 6: Illustration of different impacts of truncation on ramp filtering and 2D ATRACT filtering. From left to right: A projection of a simulated water cylinder (Image generated by Deterministic Radiological Simulation Software (DRASIM), Siemens AG, Forchheim, Germany) with the actual scan FOV indicated by the black-dashed rectangle, ramp filtering of the projection in the scan FOV, 2D ATRACT filtering of the projection in the scan FOV. Note that the filtered projection image from 2D ATRACT is almost evenly distributed while cupping-like distribution appears in the 1D ramp filtering.

the calibration information available, one of two procedures is used to deal with this problem, as follows.

Min-Max Scaling. If neither a full FOV scan is available nor the parameters in offset correction (see Eqn. (22)) are provided in the given scenario, then a simple min-max scaling method is utilized to the backprojected results, to roughly align the total intensity values to a reasonable range (-1024 ~ 3072 HU). This approach is used to avoid clamping the over-saturated values caused by an incorrect offset in the last stage of the imaging pipeline and should only be used when offset correction can not be applied.

$$f(\mathbf{x})^{corrected} = \frac{f(\mathbf{x}) - f_{min}}{f_{max} - f_{min}} \cdot 4096 - 1024 \tag{20}$$

where

$$f_{min} = \min(f(\mathbf{x}_i)) \quad \text{and} \quad f_{max} = \max(f(\mathbf{x}_i))$$

Offset Correction. If a full FOV scan is available in the related acquisition scenario or the parameters were initially calculated, then we can more effectively compensate the offset problem by calibrating the projection-related parameters in the projection domain. The correction scheme is formulated as follows:

$$g_F^{corrected}(\lambda, u, v) = g_F^{(ATRACT)}(\lambda, u, v) + \epsilon(\lambda) \tag{21}$$

$$\epsilon(\lambda) = A \cdot \sum_{u_1}^{u_2} \sum_{v_1}^{v_2} g(\lambda, u, v) + B + C \cdot (u_2 - u_1) \cdot (v_2 - v_1), \tag{22}$$

where $g_F^{(ATRACT)}(\lambda, u, v)$ and $g_F^{corrected}(\lambda, u, v)$ denote the filtered projections by ATRACT without and with correction and ϵ is the projection-dependent offset. In principle, the offset problem discussed above can also be regarded as a loss of the information on the object support. We empirically found that this information is related to the attenuation summation and truncation size. It is an interesting observation because we can approximately recover this information, i.e. $\epsilon(\lambda)$, by setting the attenuation related linear parameters A and B and truncation size related parameter C. All these parameters are calibrated by measuring the differences (offsets) between the ATRACT filtered truncated projections and the reference filtered projection by FDK from a non-truncated data.

Normally, the min-max scaling can only enable a linear relationship, rather than an exact HU value match, between the FDK reconstruction from a full FOV scan and ATRACT-based ROI reconstruction inside the ROI. The offset correction, on the other hand, is able to provide a more accurate match to that of FDK from non-truncated data.

IV. Experimental Setup

The proposed algorithms were evaluated in terms of computational efficiency and robustness of the correction quality. All data sets contain 496 projection images (1240×960) with a resolution of 0.308 mm / pixel (2×2 binning mode) that were acquired on a $200°$ short-scan circular trajectory from a C-arm system (Artis Zee, Siemens AG).

A. Measurement of Computational Performance

An open-source reconstruction benchmark framework (RabbitCT [38]) was employed to analyze the computational efficiency of the proposed methods. In this framework, the reconstruction performance is evaluated using a specific high resolution data set of a rabbit, which was acquired at the Department of Neuroradiology, University of Erlangen, Germany.

The execution time spent on processing all 496 projections with our algorithms was measured, and compared to that of a standard CPU based ramp filtering operation. Note that the Radon-based filtering in the original ATRACT used 1024 angular and 1024 of radial samples in Eqns. (2) and (3), so as to match spatial resolution.

B. Measurement of Correction Quality

To analyze the robustness of the proposed algorithms for practical application, we used two pairs of clinical examples (data courtesy of St. Luke's Episcopal Hospital, Houston, TX, USA) in presence of different types of truncation (one case additionally suffers from motion artifacts). First, we virtually collimated (by setting the outside region to 0) non-truncated projection data (see Fig. 7(a)) to three different degrees, as shown in Fig. 7(b), (c) and (d), respectively. Note that dependent on the location of the ROI, the position of virtual cropping may vary from one projection to the other.

Then, we considered two truncated clinical data sets acquired using physical X-ray collimation, namely using medium truncation (FOV area about 29% of the corresponding full data set) and using severe truncation (FOV area about 9%). The scan FOV as well as the dose area product (DAP) in

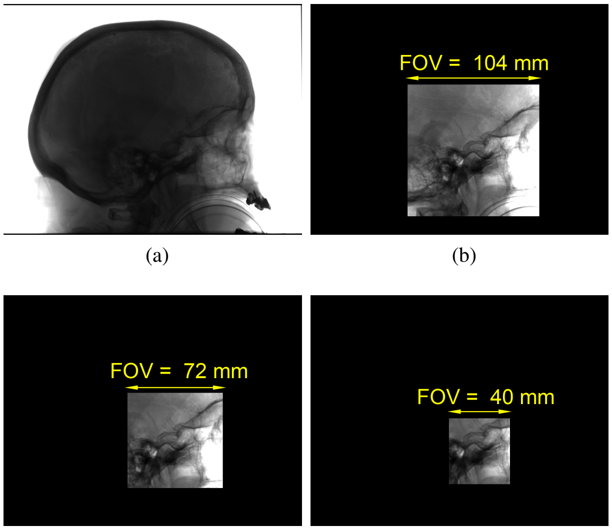

(a) (b) (c) (d)

Fig. 7: Virtual collimation of the clinical example. (a) The full FOV scan, (b)-(d) virtually cropped projections with different FOVs.

Table I: Area of FOV and DAP in the physical collimation examples.

Data set	Scan setup	FOV area (mm^2)	DAP (μGym^2)
Example 1	Full FOV	234×181	5667.4
	ROI	116×109	1630.9
Example 2	Full FOV	234×181	5676.9
	ROI	74×66	543.6

each case are listed in Table I. It should also be pointed out that the patient moved slightly in the ROI scan of Example 2. We therefore expected motion artifacts to appear in the reconstructions.

All clinical data sets were reconstructed onto a Cartesian grid ($512 \times 512 \times 350$). In the virtual collimation, the sampling spacing is $\triangle x = \triangle y = \triangle z = 0.4$ mm in all cases. In the physical collimation, the sampling spacing is $\triangle x = \triangle y = \triangle z = 0.4$ mm for the medium truncation case and $\triangle x = \triangle y = \triangle z = 0.3$ for the severe truncation case. We also investigated the performance of a refined heuristic extrapolation method [35], and compared it to our proposed algorithms. It is a hybrid extrapolation algorithm that estimates the missing data either using a water cylinder fitting scheme [20] or a Gaussian extrapolation scheme. The decision which scheme will be used depends on the slope at the truncation border, which is computed robustly from a polynomial function that was fitted to the projection data. Additionally, a transition region between measured and extrapolated data is smoothed, which reduces non-differentiable transitions and transfers noise behavior into the extrapolated range.

The standard FDK reconstruction of the full FOV scan was used as the gold standard. The ROI scans were reconstructed using the proposed corrections as well as the hybrid extrapolation method. Since the patients were repositioned in the physical collimation scans, image registrations of the reference data were performed.

C. Implementation Details

This section describes the details of the implementation of the ATRACT algorithm. The Laplace operation was computed using the finite difference method with either a 3×1 kernel (1D Laplace) or a 3×3 kernel (2D Laplace) and thus filtering can be efficiently performed in the spatial domain. The ATRACT residual filtering procedure was achieved using FFT in the Fourier domain. The kernel size was determined by the effective FOV size in the first projection: we chose the next power of 2 from the larger one among length and width of the FOV. Once the size was determined, the convolution kernel was created and applied on all projection images. To avoid singularities in the central values of the kernels (see Eqns. (12) and (17)), we estimated the central values by computing the mean value at $(u = \pm 0.1, v = \pm 0.1)$ in 2D ATRACT and $u = \pm 0.1$ in 1D ATRACT. Furthermore, the integral constant in Eqn. (18) was approximated to -0.35. Reconstruction resolution can be controlled for 2D/1D ATRACT by applying a Gaussian distribution function on the convolution kernel. For the evaluation, resolution was matched by computing the modulation transfer functions (MTF) of the 2D/1D ATRACT reconstructions and the FDK reconstruction with a Shepp-Logan filter using a bead phantom (created by DRASIM, Siemens AG, Forchheim, Germany). We applied the offset correction and chose the data in Fig. 7(a) as the reference full FOV data. It is important to state that in all evaluations the parameters A, B and C were measured only once using this reference, with $A = -3.68 \cdot 10^{-7}$, $B = 1.78$, and $C = -6.76 \cdot 10^{-7}$ in 2D ATRACT and with $A = -9.03 \cdot 10^{-8}$, $B = 1.25$ and $C = 8.48 \cdot 10^{-7}$ in 1D ATRACT. For correcting the difference of radiation due to automatic exposure control in physical collimation, we slightly adjusted the offset ϵ (subtracted by 0.2) so that HU level in the reconstruction matches the reference. Additionally, before the filtering process we set values of 30 pixels to next each boundary of the FOV to zeros, to remove the shadow of the physical collimator.

D. Image Quality Metrics

To quantify the correction accuracy obtained by each algorithm, two quantitative metrics were used.

1) Relative Root Mean Square Error (rRMSE): A simple and straightforward way to evaluate the difference of two volumes. The rRMSE gives a relative error of the evaluated volume with respect to the reference and is computed as follows

$$\mathrm{rRMSE}(f(\mathbf{x}), f^{(\mathrm{Ref})}(\mathbf{x})) = \frac{1}{f_{max}^{(\mathrm{Ref})} - f_{min}^{(\mathrm{Ref})}} \left(\frac{1}{N_{\mathrm{ROI}}} \sum_{i=0}^{N_{\mathrm{ROI}}} (f^{(\mathrm{Ref})}(\mathbf{x}_i) - f(\mathbf{x}_i))^2 \right)^{\frac{1}{2}}, \quad (23)$$

where $f^{(\mathrm{Ref})}(\mathbf{x})$ represents the reference volume, $f(\mathbf{x})$ represents the evaluated reconstructed volume and N_{ROI} indicates the number of voxels within the evaluated ROI.

2) Structural Similarity Index Measurement (SSIM): Sometimes two distorted images with same rRMSE may have very different types of error, some of which are much more perceptible for the human visual system (HVS) while others are not. SSIM is a method for measuring the similarity between two images. The biggest advantage of SSIM over the rRMSE is that it is consistent with human eye perception, modeling visual perception implicitly by regarding image contamination as a perceived change in structural information [39].

The SSIM metric of two volumes $f(\mathbf{x})$ and $f^{(\mathrm{Ref})}(\mathbf{x})$ is calculated as follows

$$\mathrm{SSIM}(f(\mathbf{x}), f^{(\mathrm{Ref})}(\mathbf{x})) = \frac{(2\mu_{\mathrm{x}}\mu_{\mathrm{Ref}} + c_1)(2\sigma_{\mathrm{x,Ref}} + c_2)}{(\mu_{\mathrm{x}}^2 + \mu_{\mathrm{Ref}}^2 + c_1)(\sigma_{\mathrm{x}}^2 + \sigma_{\mathrm{Ref}}^2 + c_2)}, \tag{24}$$

where μ_{x} and μ_{Ref} indicate the mean values of f_{x} and f_{Ref}, σ_{x}^2 and σ_{Ref}^2 indicate the variances of f_{x} and f_{Ref} and $\sigma_{\mathrm{x,Ref}}$ indicates their covariance. c_1 and c_2 are two constants to stabilize the results in case the denominator is too small (in our case, $c_1 = c_2 = 0$). The resulting SSIM ranges from -1 to +1. Large values represent good agreement in terms of both correlation and mean intensity values.

V. Results

A. Computational Efficiency

The runtimes of the filtering process for each of the algorithms are shown in Fig. 8(a). A more comprehensive comparison is represented in Fig. 8(b) by using speed-up factors with respect to the 2D Radon-based ATRACT.

As expected, a 2D Radon-based implementation of ATRACT filtering is very time-consuming (computation time is 25110 ± 116 s) due to the penalty of enormous interpolations in the non-local operation. The 2D analytical ATRACT, which uses either a numerically or an analytically derived 2D Cartesian kernel and FFT-based convolutions, reduces runtimes to 2.2% of the original version. 1D ATRACT delivers maximal computational performance, achieving an additional 5.5 times speed-up with respect to 2D ATRACT due to less computational complexity and avoidance of additional padding. We found that the 1D ATRACT filtering is only 10% slower than the ramp filtering, because it has only one additional pre-filtering step — the Laplace filtering, which is computationally inexpensive.

Further improvement in computational performance is gained by using a high-parallel graphic processing unit (GPU), the NVIDIA Quadro FX 5800. GPU versions (implemented using CUDA 4.0) of the three ATRACT methods generally reduce the runtimes to 5-6% of their CPU versions. It should be noted that the GPU version of the 2D Radon-based ATRACT is 60 times faster than its CPU version, due to beneficial utilization of texture memory which is able to implicitly handle fast linear and bi-linear interpolations.

B. Correction Quality

1) Virtual Collimation: Reconstructions from data sets shown in Fig. 7(b)-(d), i.e. of virtually collimated projection images are represented in Fig. 9 and Fig. 10. In the case of medium truncation (FOV of 104 mm and 72 mm), both 1D and 2D ATRACT, as well as the hybrid approach, produce satisfying reconstructions and avoid bright ring artifacts in the FOV. The portions of the patient inside the FOV are visually identical to the gold standard reconstruction in Fig. 9(a) and (e). Quantitative measurements, comprehended in Table II confirm this observation. With increasing degree of truncation, however, the hybrid extrapolation suffers from truncation-induced cupping artifacts at the boundaries of the FOV (see Fig. 10(b) and (f)), so that a SSIM of only 0.801 was reached in the severe truncation case (FOV of 40 mm). 2D ATRACT and 1D ATRACT, on the other hand, still maintain the reconstructions of high accuracy, which is reflected in the SSIM of 0.982 for 2D ATRACT and 0.958 for 1D ATRACT when the truncated FOV is 40 mm. The line profiles shown in Fig. 11 also demonstrate the previous observations.

2) Physical Collimation: The reconstruction results from our first physically collimated clinical data set (medium truncation) are shown in Fig. 12. Here we also use a narrow window, highlighting some mild ring-like artifacts in the hybrid extrapolation, as shown in Fig. 12(f) and (n). These artifacts — although being of small magnitude — mask the actual intensity of soft tissue in the vicinity of the FOV border. The 1D and particularly the 2D ATRACT algorithms avoid this bright ring and thus perform even slightly better in terms of soft-tissue contrast restoration, as seen in Fig. 12(g), (o) and in the central profiles shown in Fig. 14(a)-(c). These findings are confirmed by the quantitative measurements listed in Table II (FOV of 102 mm): All three correction methods yield almost identically high quality images, with 2D ATRACT only being slightly superior over the other methods.

The reconstruction results of Example 2 (severe truncation) additionally suffer from motion artifacts arising in this data set. Transversal, coronal and sagittal views through the reconstructions are given in Fig. 13 and central profiles through the transversal plane are represented in Fig. 14(d)-(f). As in the virtual collimation case, the hybrid extrapolation method results in more severe truncation artifacts from the heavily truncated data; see Fig. 13(f) and (j). Quantitatively, 2D ATRACT yields the most accurate result, with an rRMSE of only half of that of the hybrid extrapolation scheme (see Table II (FOV of 65 mm)). Performance of the 1D ATRACT lies between them, achieving an rRMSE of 6.82% and an SSIM of 0.718.

VI. Discussion

In this paper, we presented and evaluated two variants of a truncation correction algorithm recently suggested for interventional 3D ROI imaging. The general algorithmic scheme of our method is different from that of other methods proposed in the field.

Methods that require prior knowledge (e.g. [11], [17] and [18]) can only be applied in a clinical workflow that generates such information. Our scope of application, however, is a clinical angiography system that is used for a variety of workflows. In some of them a full scan is generated during a procedure. In others such data are not available. Thus, we

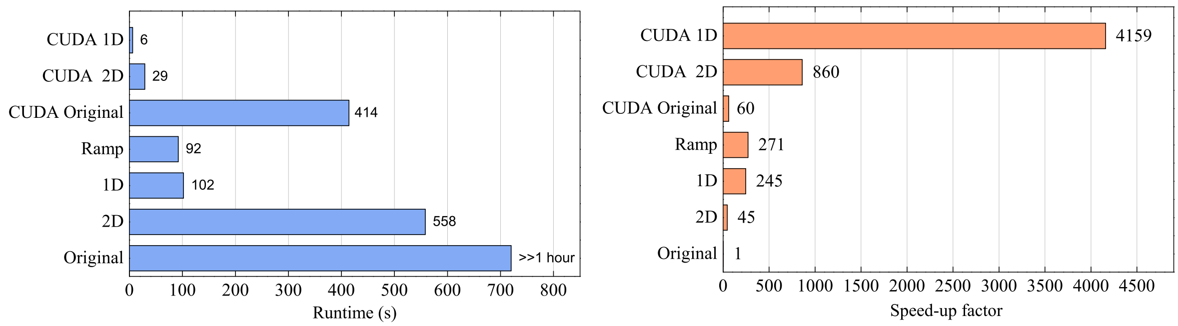

(a) (b)

Fig. 8: Runtime (a) and speed-up factor (b) of filtering 496 projections (1240×960) for each algorithm. "Original" stands for the direct implementation of the Radon-based filtering in the original ATRACT algorithm. "2D" represents the CPU implementation of 2D ATRACT with 2D analytical convolution filtering. "1D" corresponds to the CPU implementation of 1D ATRACT. The corresponding GPU versions of these algorithms are labeled as "CUDA Original", "CUDA 2D", and "CUDA 1D", respectively. A NVIDIA Quadro FX 5800 was used for GPU implementations, CUDA version 4.0. CPU implementations were based on a single-threaded Intel® Xeon X5570.

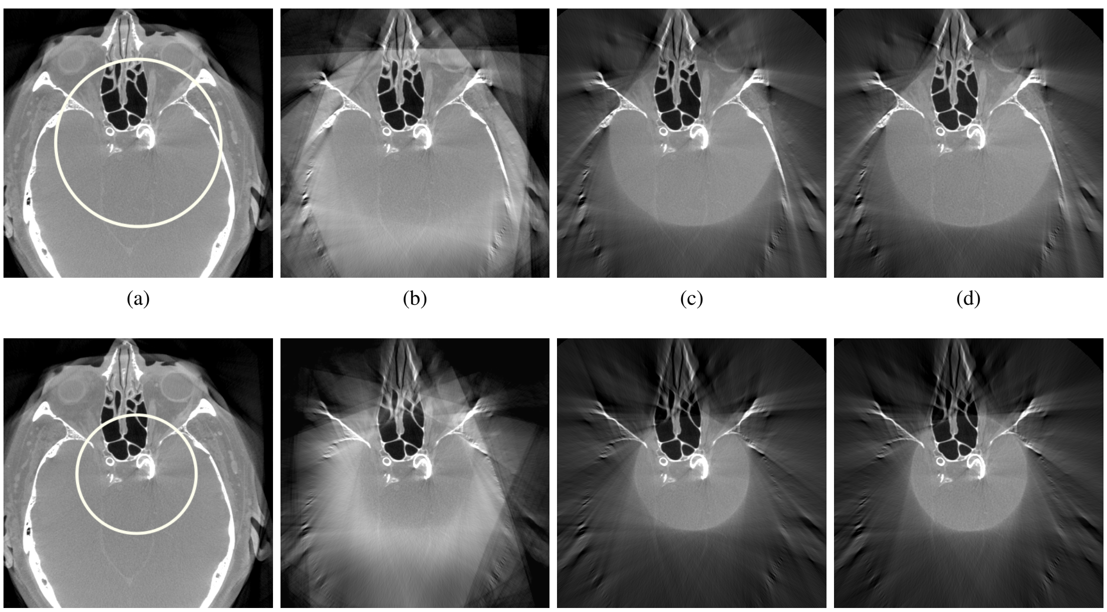

(a) (b) (c) (d)

(e) (f) (g) (h)

Fig. 9: Reconstructions of the clinical data set from the virtual collimation, in the grayscale window [-1000 HU, 1000 HU]. From left to right: Gold standard FDK reconstruction from non-truncated projection, hybrid extrapolation-based ROI reconstruction, 2D ATRACT-based ROI reconstruction, 1D ATRACT-based ROI reconstruction. (b)-(d): ROI reconstructions from the FOV of 104 mm, (f)-(h): ROI reconstructions from the FOV of 72 mm. The white circles in the gold standard reconstructions indicate the ROIs.

Table II: Summary of quantitative evaluation of truncation corrections for different FOVs in virtual collimation as well as physical collimation.

		Virtual collimation			Physical collimation	
Algorithms	Metrics	FOV 104 mm	FOV 72 mm	FOV 40 mm	FOV 102 mm	FOV 65 mm
Hybrid extrapolation	rRMSE (%)	1.15	3.15	9.13	1.82	11.4
	SSIM	0.972	0.944	0.801	0.940	0.695
2D ATRACT	rRMSE (%)	0.922	0.923	0.974	1.65	5.19
	SSIM	0.987	0.979	0.982	0.945	0.785
1D ATRACT	rRMSE (%)	1.28	1.08	2.70	1.68	6.82
	SSIM	0.978	0.978	0.958	0.943	0.718

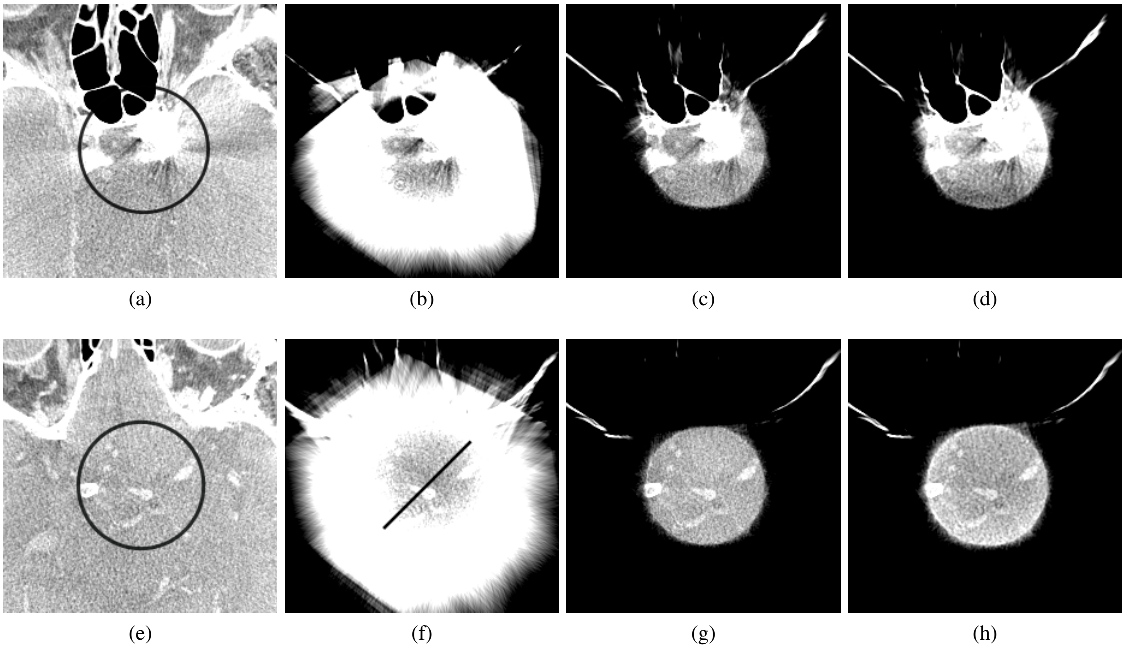

Fig. 10: Two transversal slices through the reconstructions of the clinical data set from the virtual collimation with the FOV of 40 mm, in the grayscale window [-200 HU, 200 HU]. From left to right: Gold standard FDK reconstruction from non-truncated projection, hybrid extrapolation-based ROI reconstruction, 2D ATRACT-based ROI reconstruction, 1D ATRACT-based ROI reconstruction. The black circles in the gold standard reconstructions indicate the ROIs. For a fair comparison, remaining offsets were manually subtracted from the reconstructed results of the three methods.

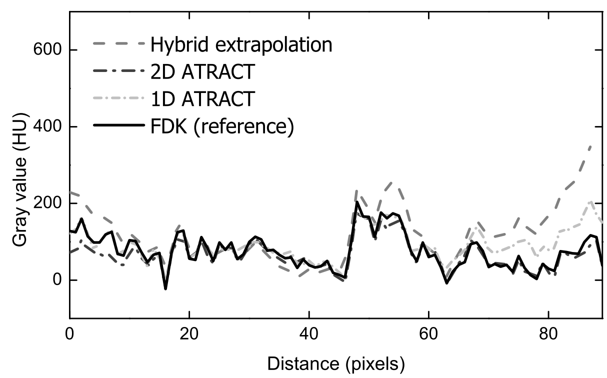

Fig. 11: Plots of the line profiles indicated as the black solid line in the transversal slice (Fig. 10) for each algorithm. It can be seen that the cupping artifact still remains in the hybrid method but is effectively reduced in the ATRACT methods, particularly in 2D ATRACT.

wanted to create a robust method that is able to be applicable to all workflows that are performed on such a machine. The ATRACT method fulfills this requirement and is able to deal with all these clinical constraints. Also, it only requires the ROI itself to be irradiated from all necessary views. Thus, this is different from the algorithms which deploy a non-uniform beam filter between the X-ray source and the patient and which circumvent the truncation problem but at the cost of reducing the benefit of dose reduction and complicating the data acquisition due to additional hardware ([14]-[16]). The difference in dose reduction can be even considerable in the field of neuroradiology where only a micro device, e.g. an implanted stent or coil, is required to be examined multiple times. Compared to the iterative methods proposed in [26] and [27] or the PI-line-based BPF algorithms in [12] and [13] (computing the PI-lines is time-consuming), the new methods adopt the filtered backprojection scheme and can be directly applied in clinically used scanners at low computational cost. Explicit extrapolation methods ([20]-[25]) are commercially preferred since they are computationally efficient and are able to estimate the missing data heuristically without the requirement of prior knowledge. They may be, however, difficult to apply to severe truncations that are encountered in ROI scans. In the evaluation, our methods were compared to a refined hybrid extrapolation method [35] both qualitatively and quantitatively, and showed for the clinical data superior results in the severe truncation cases. These results are thus in line with previous findings reported in [28], [29] and imply that our algorithms are capable of delivering higher quality images for severe truncation problems with considerable reduction of patient dose of up to 90% or more.

Moreover, it is noted that recent appealing techniques

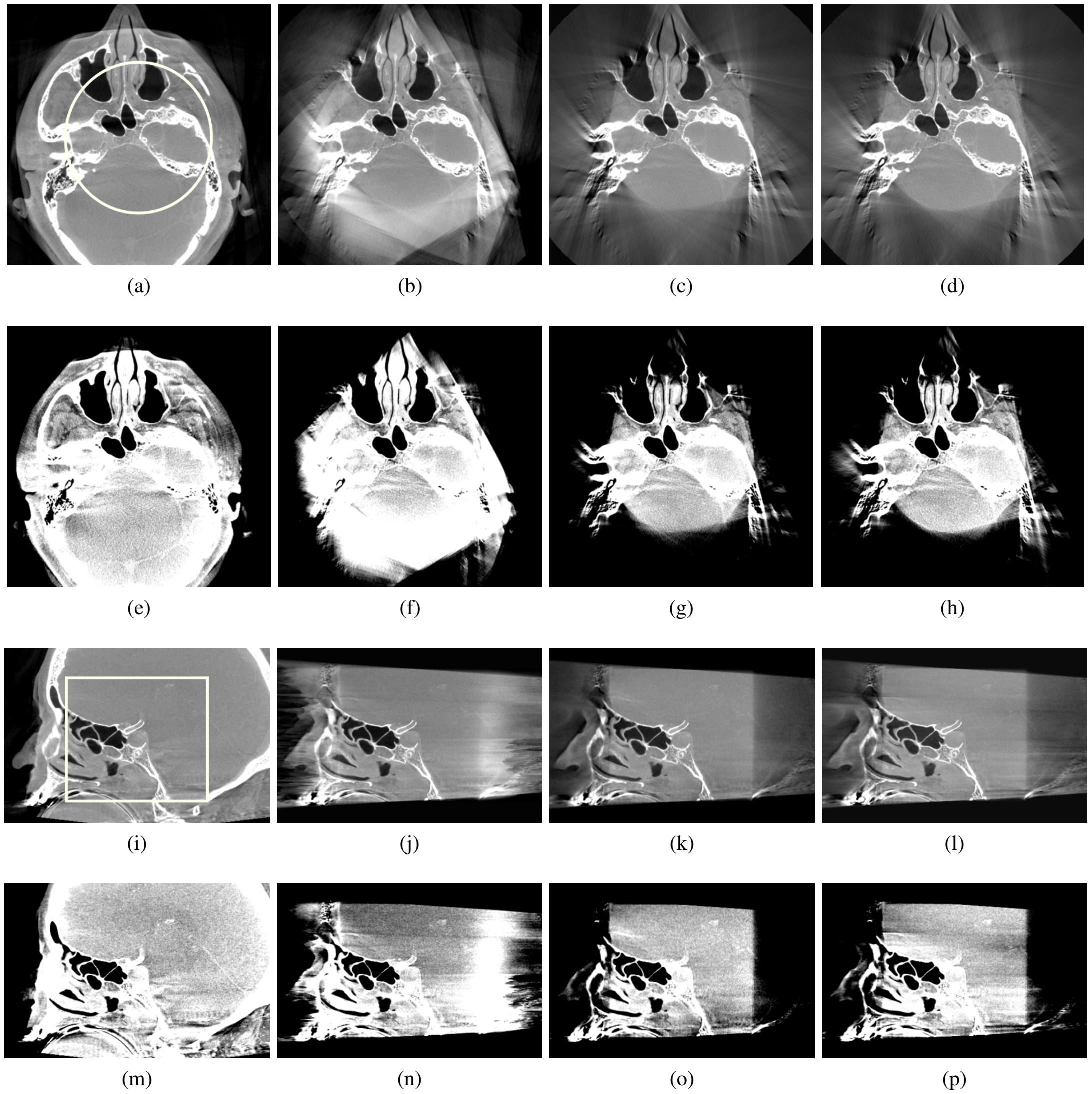

Fig. 12: Reconstruction results of the clinical example 1 by the three algorithms. From left column to right column: Gold standard FDK reconstruction from non-truncated projection data, hybrid extrapolation-based ROI reconstruction, 2D ATRACT-based ROI reconstruction, 1D ATRACT-based ROI reconstruction. (a)-(h): Transversal view, (i)-(p): Sagittal view. (a)-(d) and (i)-(l) are in the grayscale window [-1000 HU, 1000 HU], (e)-(h) and (m)-(p) are in the grayscale window [-200 HU, 200 HU]. The white circle and rectangle in the gold standard reconstructions indicate the ROIs.

such as dynamic asymmetric collimation [40] will make ROI imaging more flexible but results in off-center FOVs in the projection data. Some algorithms mentioned above ([12], [14]-[16], [21]-[23]) may encounter problems in such a scenario. Although not described in detail here, the ATRACT method also has been demonstrated to be handle off-center ROI reconstructions [31].

The evaluation results show that the new ATRACT methods significantly outperform the Radon-based version in terms of computational performance. Since no explicit extrapolation of projection data is involved, the proposed methods have the potential to minimize the computational requirements for processing truncated data. As mentioned in Section IV-C, the convolution kernel can be adapted to the effective FOV size. For the projection images that are truncated to 222 pixels in each row, it is sufficient to create the convolution kernel with a size of 512 pixels and then pad the images to 512 pixels. For the heuristic extrapolation methods (e.g. water cylinder extrapolation), the ramp kernel is convolved with the extrapolated row (sometimes 1240 pixels in our case), even if the data are highly truncated. This means the 1D FFT of an ROI image in physical collimation example 2 (222×192 pixels) requires computational complexity of $192 \cdot 2048 \log_2 2048$ for the water cylinder extrapolation compared to a complexity of $192 \cdot 512 \log_2 512$ for the 1D ATRACT method.

Apart from the computational speed-up, another improvement of the ATRACT method is the offset correction described in Section III-E. With this correction, the HU values can be used again for bone or soft tissue segmentation if some tolerance is accepted. Additional impact is to support any volume-based post-processing algorithm in final stages of the imaging pipeline that relies on absolute HU values in the reconstructed volume. Although the requirement is a full FOV scan, it is substantially different from the prior knowledge used

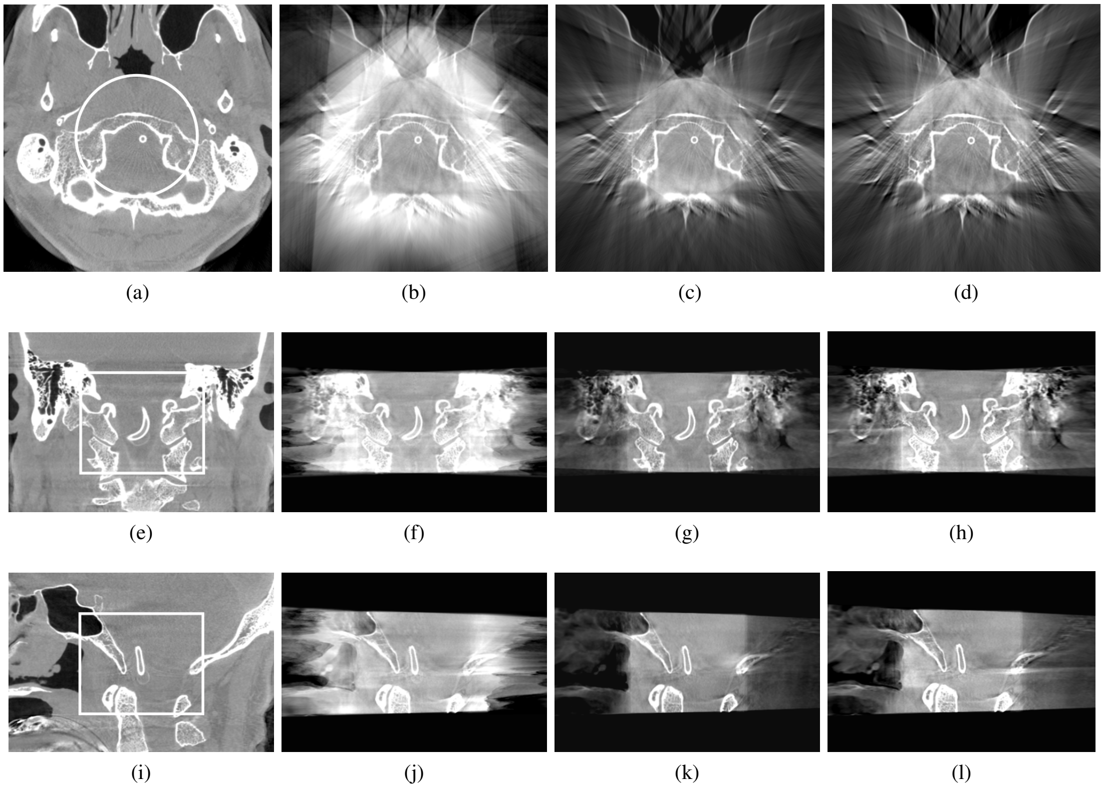

Fig. 13: Reconstruction results of the clinical example 2 by the three algorithms, in the grayscale window [-1000 HU, 1000 HU]. From left column to right column: Gold standard FDK reconstruction from non-truncated projection data, hybrid extrapolation-based ROI reconstruction, 2D ATRACT-based ROI reconstruction, 1D ATRACT-based ROI reconstruction. (a)-(d): Transversal view, (e)-(h): Coronal view, (i)-(l): Sagittal view. The white circle and rectangles in the gold standard reconstructions indicate the ROIs.

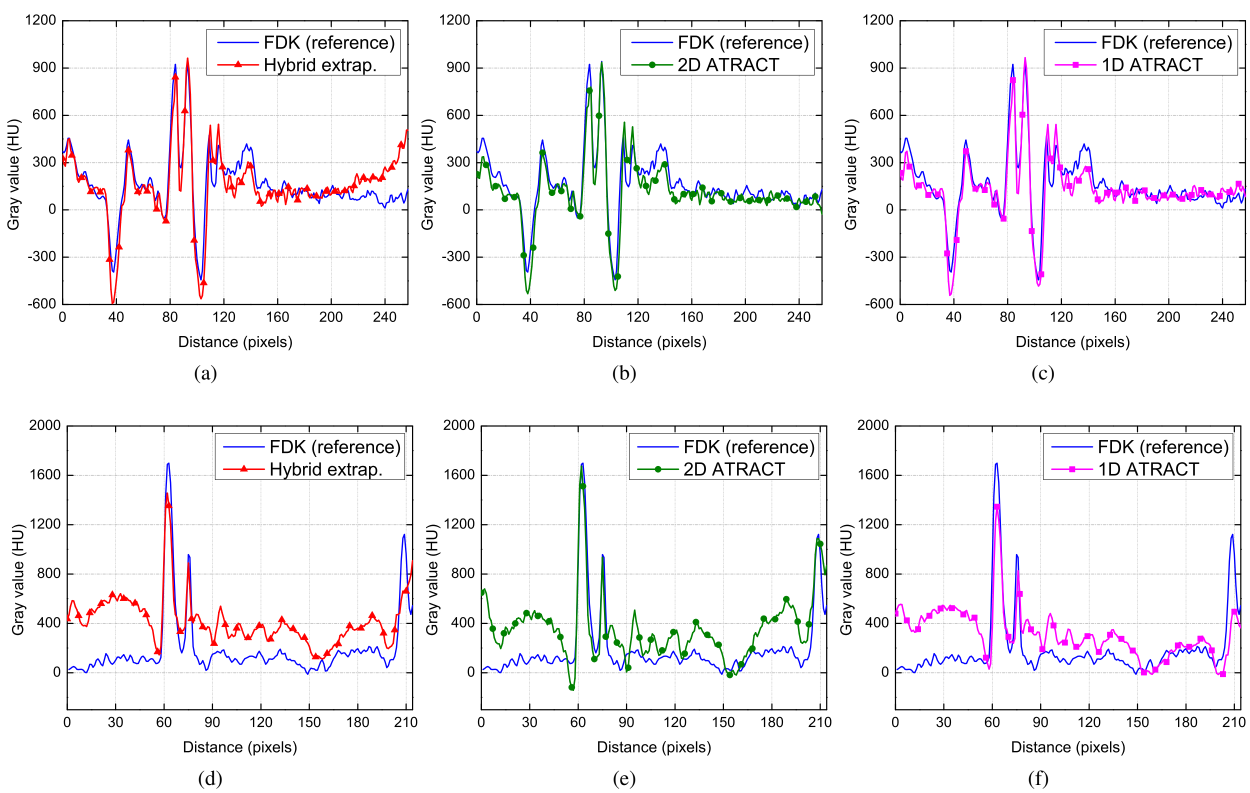

Fig. 14: Plots of central line profile in the transversal slice for each algorithm. (a)-(c): clinical example 1, (d-f): clinical example 2.

in [8]-[11], [17], [18] for two reasons: The full FOV scan is employed as a reference for offset correction, instead of completing data for truncation correction; Determination of the parameters in Eqn. (22) is required only once, working as an initialization or a calibration measurement for a given scenario. This measurement does not even have to be performed if using the same acquisition system. The calibration parameters can be factory preset for a given organ program at the scanner. We also investigated more clinical data sets in virtual collimation acquired from the same acquisition system and an average rRMSE of 1.63% (including truncation artifacts) was achieved [33]. The limitation is that only patient head data sets were employed in this work. We assume that differences in patient anatomy are likely to result in variations of the correction parameters. When the reference scan is not available, a min-max scaling approach is used for approximation of the HU values in a reasonable range. In such case, a different display window is required for the visual inspection and quantitative evaluation becomes more cumbersome.

For image quality evaluation of the proposed methods, we involved physically collimated data and also the virtual collimation, as introduced in [29], since the latter nicely allows retrospective adjustment of the degrees of collimation for early studies. Quantitative measurements using the rRMSE and the SSIM in the physical collimation are generally inferior to those obtained with virtual collimation, most probably caused by the differences in data acquisition, data pre-processing, the level of physical effects and motion.

VII. Conclusion

In conclusion, we adapted the ATRACT method for clinical use and showed real data reconstructions. Adapting convolution-based filtering, the use of GPUs and the optional switch to 1D processing yielded implementations that are efficient with runtimes that are clinically feasible. Speed-up factors of up to 245 were observed, compared to a direct implementation of 2D Radon-based filtering. Image quality evaluation on clinical data demonstrated that our methods performed at least as well as a state-of-the art hybrid extrapolation method. However, while the hybrid extrapolation scheme behaves worse with increasing degree of truncation, our new methods (especially 2D ATRACT) showed no significant dependence of reconstruction accuracy on the size of the FOV. The potential of our approaches for interventional 3D ROI imaging is therefore attractive for two reasons: They have comparable computational efficiency to the FDK algorithm and high capability to achieve accurate ROI reconstruction from severely truncated data. Future work will comprise validation in a larger study. The present paper, however, indicates that the current algorithms will meet all clinical constraints regarding computational speed, flexibility, and image quality.

Appendix

The frequency representation of the 2D analytic kernel can be obtained by the 2D Fourier transform of h_{2D} (see Eqn (12)):

$$H_{2D}\left(\omega_u,\omega_v\right)=\int_{-\infty}^{-\infty}\int_{-\infty}^{-\infty}\frac{|v|}{u^2+v^2}e^{-i2\pi(u\omega_u+v\omega_v)}\mathrm{d}u\mathrm{d}v\,, \quad (25)$$

where ω_u and ω_v are spatial frequencies of u and v, respectively. Eqn (25) can be solved by integration with respect to u and then followed by integration with respect to v:

$$H_{2D}\left(\omega_u,\omega_v\right)=\int_{-\infty}^{-\infty}\left[\int_{-\infty}^{-\infty}\frac{|v|}{u^2+v^2}e^{-i2\pi u\omega_u}\mathrm{d}u\right]e^{-i2\pi v\omega_v}\mathrm{d}v\,. \quad (26)$$

The innermost integral yields the 1D Fourier transform of $\frac{|v|}{u^2+v^2}$ with respect to u. Then we can solve it using the duality property of the Fourier transform (if $\mathcal{F}\left[f\left(t\right)\right]=X\left(\omega\right)$, then $\mathcal{F}\left[X\left(t\right)\right]=f\left(-\omega\right)$):

It is well-known that the Fourier transform of $f\left(t\right)=e^{-a|t|}$ yields

$$\mathcal{F}(e^{-a|t|})=\frac{2a}{a^2+\omega^2}\,. \quad (27)$$

Using the property of duality of the Fourier transform, it then follows that

$$\mathcal{F}(\frac{2a}{a^2+t^2})=e^{-a|\omega|}\,. \quad (28)$$

Thus, the 1D Fourier transform of $\frac{|v|}{u^2+v^2}$ with respect to u is

$$\mathcal{F}(\frac{|v|}{v^2+u^2})=\frac{1}{2}e^{-|v||\omega_u|}\,. \quad (29)$$

Furthermore, outermost integration of (26) is the 1D Fourier transform of $\frac{1}{2}e^{-|v||\omega_u|}$ with respect to v. This can be computed by re-using Eqn (27):

$$\mathcal{F}(\frac{1}{2}e^{-|\omega_u||v|})=\frac{|\omega_u|}{\omega_u^2+\omega_v^2}\,. \quad (30)$$

Therefore, we get the frequency representation of the analytical 2D kernel:

$$H_{2D}\left(\omega_u,\omega_v\right)=\frac{|\omega_u|}{\omega_u^2+\omega_v^2}\,. \quad (31)$$

Acknowledgment

The authors gratefully acknowledge funding by Siemens AG, Healthcare Sector and of the Erlangen Graduate School in Advanced Optical Technologies (SAOT) by the German Research Foundation (DFG) in the framework of the German excellence initiative. The authors also would like to thank Dr. Mawad in St. Luke's Episcopal Hospital for providing the valuable clinical data sets. All reconstruction results were computed with a Siemens prototype software, not a clinical product. The concepts and information presented in this paper are based on research and are not commercially available.

REFERENCES

[1] N. Strobel, O. Meissner, J. Boese, T. Brunner, B. Heigl, M. Hoheisel, G. Lauritsch, M. Nagel, M. Pfister, E.-P. Ruehrnschopf, B. Scholz, B. Schreiber, M. Spahn, M. Zellerhoff, and K. Klingenbeck-Regn, *Imaging with Flat-Detector C-Arm Systems*, ser. Multislice CT. Springer, 2008.

[2] U. Missler, C. Hundt, M. Wiesmann, T. Mayer, and H. Brueckmann, "Three-dimensional reconstructed rotational digital subtraction angiography in planning treatment of intracranial aneurysms," *European Radiology*, vol. 10, no. 4, pp. 564–568, 2000.

[3] A. Hochmuth, U. Spetzger, and M. Schumacher, "Comparison of three-dimensional rotational angiography with digital subtraction angiography in the assessment of ruptured cerebral aneurysms," *American Journal of Neuroradiology*, vol. 23, no. 7, pp. 1199–1205, 2002.

[4] T. Sugahara, Y. Korogi, K. Nakashima, S. Hamatake, S. Honda, and M. Takahashi, "Comparison of 2D and 3D digital subtraction angiography in evaluation of intracranial aneurysms," *American Journal of Neuroradiology*, vol. 23, no. 9, pp. 1545–1552, 2002.

[5] R. Fahrig, R. Dixon, T. Payne, R. L. Morin, A. Ganguly, and N. Strobel, "Dose and image quality for cone-beam C-arm CT system," *Medical Physics*, vol. 33, no. 12, pp. 4541–4550, 2006.

[6] F. Noo, R. Clackdoyle, and J. D. Pack, "A Two-step Hilbert Transform Method for 2D Image Reconstruction," *Physics in Medicine and Biology*, vol. 49, no. 17, pp. 3903–3923, 2004.

[7] X. Pan, Y. Zhou, and D. Xia, "Image reconstruction in peripheral and central region-of-interest and data redundancy," *Medical Physics*, vol. 32, no. 3, pp. 673–684, 2005.

[8] M. Defrise, F. Noo, R. Clackdoyle, and H. Kudo, "Truncated Hilbert transform and image reconstruction from limited tomographic data," *Inverse Problems*, vol. 22, no. 3, pp. 1037–1053, 2006.

[9] Y. Ye, H. Yu, and G. Wei, "Exact interior reconstruction with cone-beam CT," *International Journal of Biomedical Imaging*, vol. 2007, p. 10693, 2007.

[10] ——, "Exact interior reconstruction from truncated limited-angle projection data," *International Journal of Biomedical Imaging*, vol. 2008, p. 427989, 2008.

[11] H. Kudo, M. Courdurier, F. Noo, and M. Defrise, "Tiny a priori knowledge solves the interior problem in computed tomography," *Physics in Medicine and Biology*, vol. 52, no. 9, p. 2207, 2008.

[12] L. Yu, E. Y. Sidky, C. A. Pelizzari, P. Munro, and X. Pan, "Region of interest reconstruction from truncated data in circular cone-beam CT," *IEEE Transactions on Medical Imaging*, vol. 25, no. 7, pp. 869–881, 2006.

[13] S. Cho, J. Bian, C.-T. Pelizzari, C. A.and Chen, T.-C. He, and X. Pan, "Region-of-interest reconstruction in circular cone-beam microCT," *Medical Physics*, vol. 34, no. 12, pp. 4923–4933, 2007.

[14] R. Chityala, K. R. Hoffmann, D. R. Bednarek, and S. Rudin, "Region of Interest (ROI) Computed Tomography," *Proceedings of Society Photo-Optical Instrumentation Engineers*, vol. 5368, no. 2, pp. 534–541, 2004.

[15] L. Chen, C. C. Shaw, M. C. Altunbas, C. J. Lai, X. Liu, T. Han, T. Wang, W. T. Yang, and G. J. Whitman, "Feasibility of volume-of-interest (VOI) scanning technique in cone beam breast CT - A preliminary study," *Medical Physics*, vol. 35, no. 8, pp. 3482–3490, 2008.

[16] S. Schafer, P. B. Noel, A. Walczak, and K. Hoffmann, "Filtered region of interest cone-beam rotational angiography," *Medical Physics*, vol. 37, no. 2, pp. 694–703, 2010.

[17] D. Kolditz, Y. Kyriakou, and W. A. Kalender, "Volume-of-interest (VOI) imaging in C-arm flat-detector CT for high image quality at reduced dose," *Medical Physics*, vol. 37, no. 6, pp. 2719–2730, 2010.

[18] D. Kolditz, M. Meyer, Y. Kyriakou, and W. A. Kalender, "Comparison of extended field-of-view reconstructions in C-arm flat-detector CT using patient size, shape or attenuation information," *Physics in Medicine and Biology*, vol. 56, no. 1, pp. 39–56, 2011.

[19] B. Ohnesorge, T. Flohr, K. Schwarz, J. P. Heiken, and J. P. Bae, "Efficient correction for CT image artifacts caused by objects extending outside the scan field of view," *Medical Physics*, vol. 27, no. 1, pp. 39–46, 2000.

[20] J. Hsieh, E. Chao, J. Thibault, B. Grekowicz, A. Horst, S. McOlash, and T. J. Myers, "A novel reconstruction algorithm to extend the CT scan field-of-view," *Medical Physics*, vol. 31, no. 9, pp. 2385–2391, 2004.

[21] J. D. Maltz, S. Bose, H. P. Shukla, and A. R. Bani-Hashemi, "CT truncation artifact removal using water-equivalent thicknesses derived from truncated projection data," in *IEEE Engineering in Medicine and Biology Society*, 2007, pp. 2905–2911.

[22] G. Van Gompel, G. Tisson, D. Van Dyck, and J. Sijbers, "A new algorithm for 2D region of interest tomography," in *Proceedings of SPIE 5370*, 2004, pp. 2105–2113.

[23] K. Sourbelle, M. Kachelriess, and W. A. Kalender, "Reconstruction from truncated projections in CT using adaptive detruncation," *European Radiology*, vol. 15, no. 5, pp. 1008–1014, 2005.

[24] A. Maier, B. Scholz, and F. Dennerlein, "Optimization-based Extrapolation for Truncation Correction," in *2nd CT Meeting*, 2012, pp. 390–394.

[25] B. Bier, A. Maier, H. Hofmann, C. Schwemmer, Y. Xia, T. Struffert, and J. Hornegger, "Truncation correction for VOI C-arm CT using scattered radiation," in *Proceedings of SPIE*, 2013, p. 86682F9.

[26] H. Yu and G. Wang, "Compressed sensing based interior tomography," *Physics in Medicine and Biology*, vol. 54, no. 9, pp. 2791–2805, 2009.

[27] J. Yang, H. Yu, M. Jiang, and G. Wang, "High-order total variation minimization for interior tomography," *Inverse problems*, vol. 26, no. 3, p. ID: 035013, 2010.

[28] F. Dennerlein, "Cone-beam ROI reconstruction using the Laplace operator," in *Proceedings of Fully 3D 2011*, 2011, pp. 80–83.

[29] F. Dennerlein and A. Maier, "Region-of-interest reconstruction on medical C-arms with the ATRACT algorithm," in *Proceedings of SPIE*, 2012, p. 83131B.

[30] ——, "Approximate truncation robust computed tomography - ATRACT ," *Physics in Medicine and Biology*, vol. 58, pp. 6133–6148, 2013.

[31] Y. Xia, A. Maier, F. Dennerlein, H. G. Hofmann, and J. Hornegger, "Efficient 2D filtering for cone-beam VOI reconstruction," in *IEEE Nuclear Science Symposium and Medical Imaging Conference*, 2012, pp. 2415–2420.

[32] Y. Xia, A. Maier, F. Dennerlein, H. Hofmann, K. Mueller, and J. Hornegger, "Reconstruction from truncated projections in cone-beam CT using an efficient 1D filtering," in *Proceedings of SPIE*, 2013, p. 86681C.

[33] Y. Xia, A. Maier, F. Dennerlein, H. Hofmann, and J. Hornegger, "Scaling Calibration in the ATRACT Algorithm," in *Proceedings Bildverarbeitung fuer die Medizin 2013*, 2013, pp. 104–109.

[34] A. Maier, Z. Jiang, J. Jordan, C. Riess, H. Hofmann, and J. Hornegger, "Atlas-Based Linear Volume-of-Interest (ABL-VOI) Image Correction," in *Proc. SPIE*, vol. 8668, 2013, p. 86682D.

[35] B. Zellerhoff, B. Scholz, E. P. Ruehrnschopf, and T. Brunner, "Low contrast 3D-reconstruction from C-arm data," in *Proceedings of SPIE*, 2005, pp. 646–655.

[36] L. A. Feldkamp, L. C. Davis, and J. W. Kress, "Practical cone beam algorithm," *Optical Society of America*, vol. 1, pp. 612–619, 1984.

[37] A. V. Bronnikov, "Phase-contrast CT: Fundamental theorem and fast image reconstruction algorithms," in *Proceedings of SPIE*, 2006, p. 63180Q.

[38] C. Rohkohl, B. Keck, H. G. Hofmann, and J. Hornegger, "RabbitCT—an open platform for benchmarking 3D cone-beam reconstruction algorithms," *Medical Physics*, vol. 36, no. 9, pp. 3940–3944, 2009.

[39] Z. Wang, A. C. Bovik, H. R. Sheikh, and E. P. Simoncelli, "Image quality assessment: from error visibility to structural similarity," *IEEE Transactions on Image Processing*, vol. 13, no. 4, pp. 600–612, April 2004.

[40] D. Heuscher and F. Noo, "CT dose reduction using dynamic collimation," in *IEEE Nuclear Science Symposium and Medical Imaging Conference*, 2011, pp. 3470–3473.